CAMM
Center for Advanced Microelectronics Manufacturing
BINGHAMTON UNIVERSITY

BINGHAMTON UNIVERSITY
STATE UNIVERSITY OF NEW YORK

S3IP
A New York State Center of Excellence
BINGHAMTON UNIVERSITY

NEXTFLEX

iMAPS New England Chapter
International Microelectronics Assembly and Packaging Society
45th Symposium & Expo - May 1, 2018, Boxborough, MA, USA

In Situ Functional Monitoring of Aerosol Jet-Printed Electronics

Roozbeh (Ross) Salary
Ph.D. Candidate, Speaker

Jack P. Lombardi
Ph.D. Candidate

Darshana L. Weerawarne
Ph.D., Postdoctoral Associate

M. Samie Tootooni
Ph.D., Postdoctoral Associate

Prahalad K. Rao
Ph.D., Assistant Professor

Mark D. Poliks
Ph.D., Professor

Outline

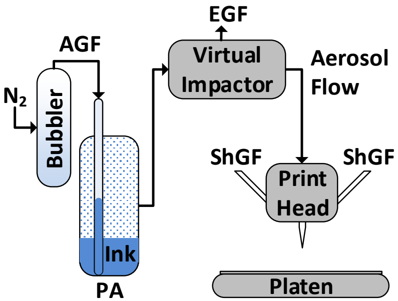

1 An Introduction to AJP

2 Sensor-Instrumented Experimental Setup

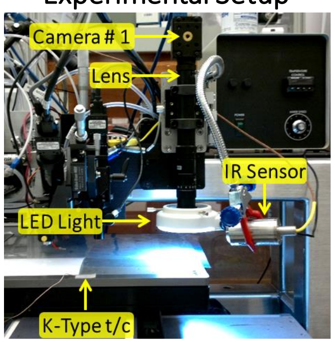

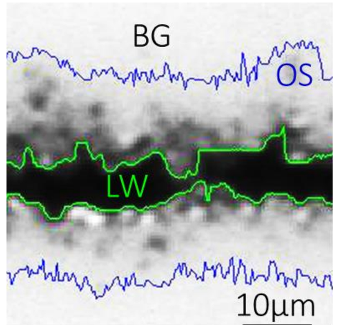

3 2D Quantification of Line Morphology

4 Computational Fluid Dynamics Modeling

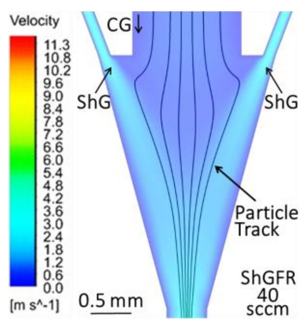

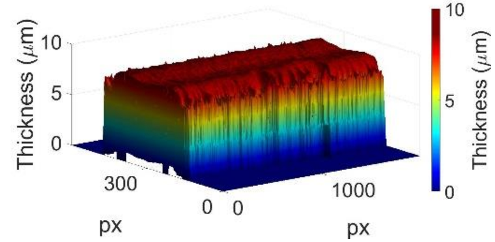

5 3D Quantification of Line Morphology

6 *In Situ* Estimation of Line Resistance

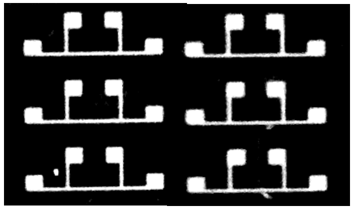

Aerosol Jet Printing (AJP)

AJP is a direct-write (DW) additive manufacturing (AM) technique, used for manufacture of electronic devices.

Hon, K., *et al*., CIRP Annals-Manufacturing Technology, **57**(2), pp. 601-620 (2008).

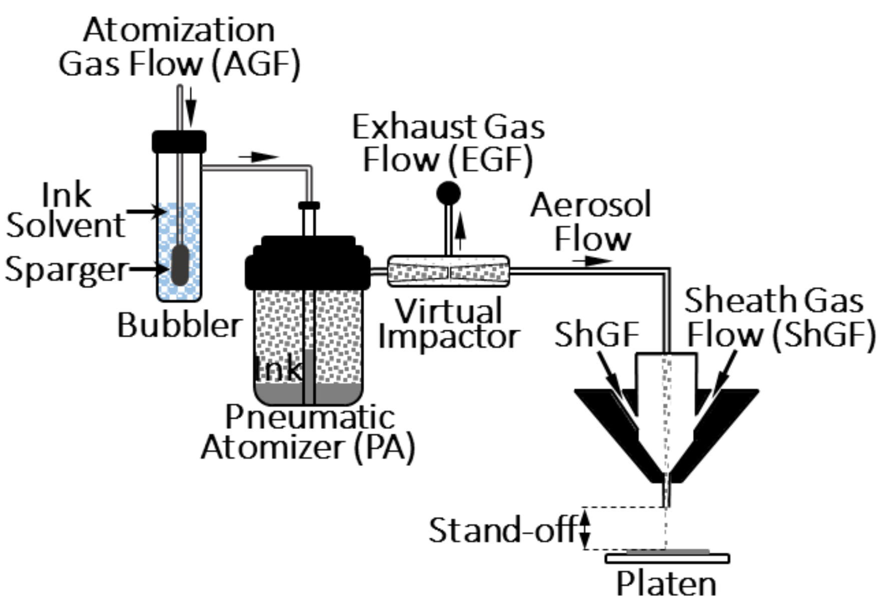

Salary, R., *et al*., ASME-MSEC 2018, Texas A&M University, College Station, TX, USA, June 18-22, 2018.

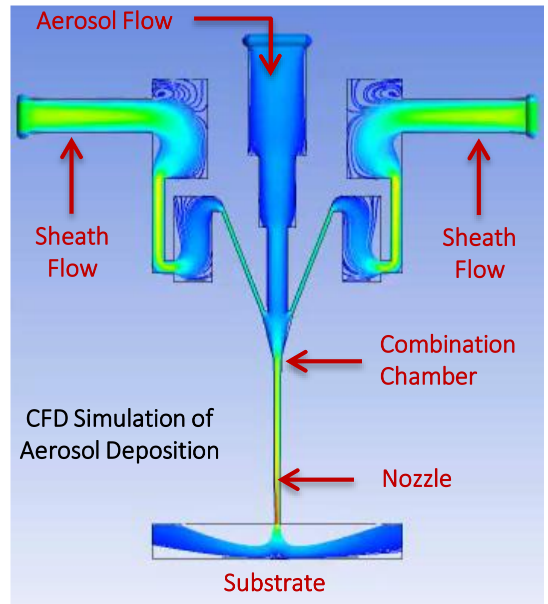

Salary, R., *et al*., 2016, ASME-JMSE, 139(2), p. 021015.

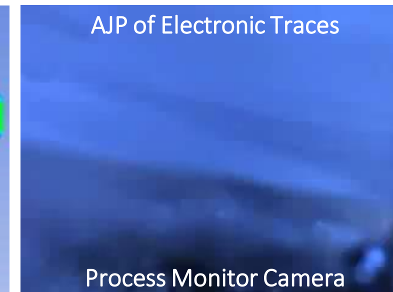

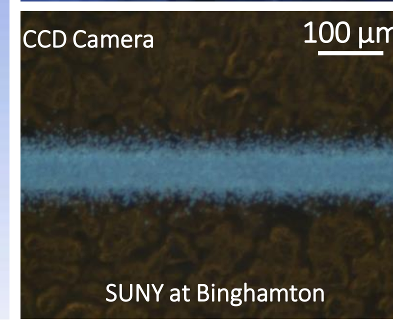

AJP allows for low-temperature, high-resolution fabrication of electronics (≤10 µm), accommodating a wide range of ink viscosity (0.7-2500 cP).

Hon, K., *et al*., CIRP Annals-Manufacturing Technology, **57**(2), pp. 601-620 (2008).
Parekh, D. *et al*., Additive Manufacturing (Chapter 8), CRC Press, Boca Raton, Florida, p. 215., 2015.

Aerosol Jet Printing of Electronic Devices

AJP has been used for fabrication of supercapacitors, inter-digitated electrodes, antennas, biosensors, etc.

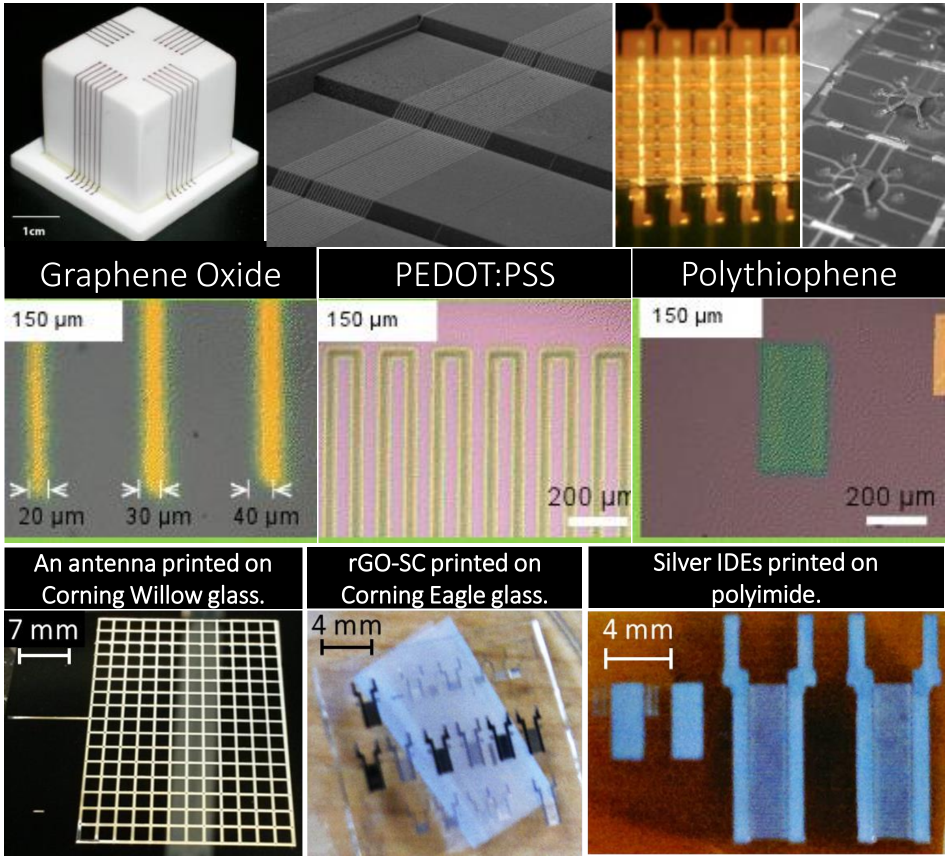

Hedges, M., *et al*., DDMC, Berlin, Germany, Mar. 14–15, 2012, pp. 14–15.
King, B., *et al*., Lockheed Martin Palo Alto Colloquia, Palo Alto, CA, 2009.
Salary, R., *et al*., 2016, Journal of Manufacturing Science and Engineering, 139(2), p. 021015.

Novel solution-based materials, such as metal nanoparticles, graphene oxide, and PEDOT:PSS can be deposited.

Nonlinear and Nonstationary Behavior of AJP

There are process-material-machine interactions which swerve the AJP process off any pre-defined optimal window.

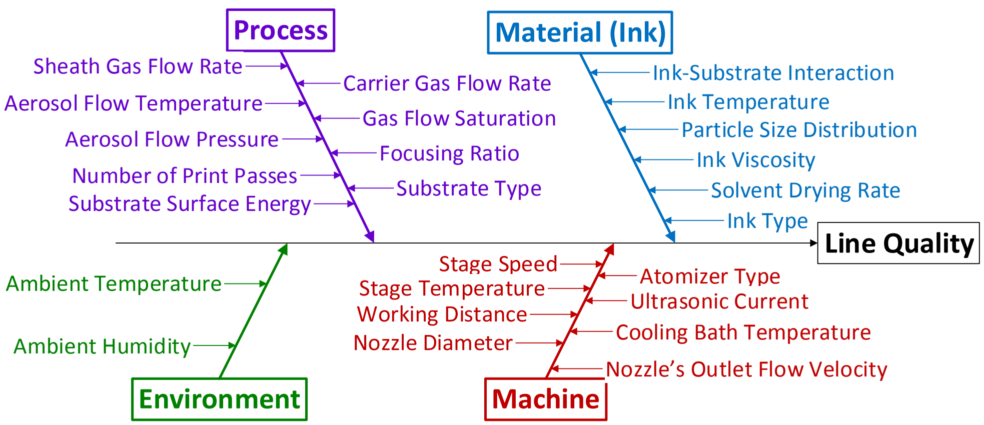

Salary, R., *et al.*, ASME-MSEC 2016, Vol. 2, Virginia Tech, Blacksburg, VA, USA, June 27-July 1, 2016.

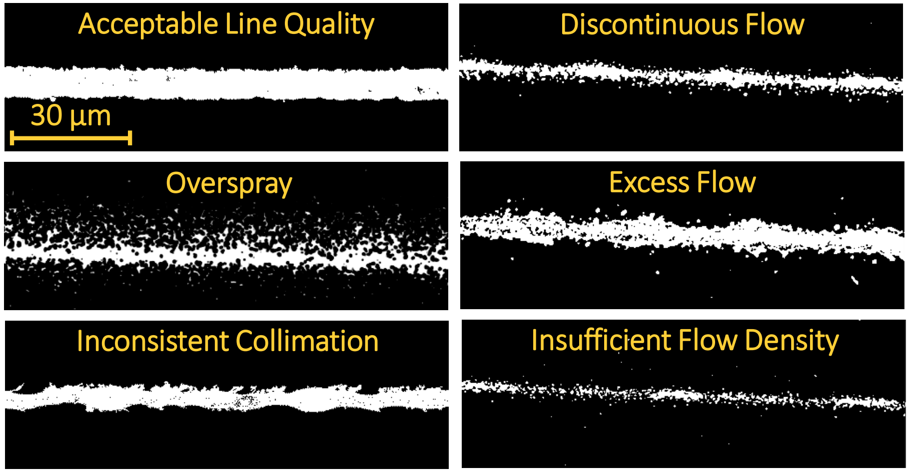

Salary, R., *et al.*, 2016, Journal of Manufacturing Science and Engineering, 139(2), p. 021015.

AJP is intrinsically unstable and prone to gradual drifts. Hence, real-time monitoring and closed-loop control are bourgeoning needs.

Goal:

Real-time functional monitoring of AJ-printed electronic devices.

Objectives:

(1) *In situ* image acquisition from the traces of a device right after deposition.

(2) *In situ* image processing and quantification of trace morphology.

(3) *In situ* estimation of the device functional properties, using a supervised machine learning model.

(4) CFD modeling of AJP to explain the underlying aerodynamic phenomena behind aerosol transport and deposition.

Outline

1 An Introduction to AJP

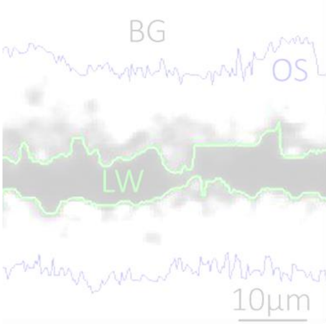

3 2D Quantification of Line Morphology

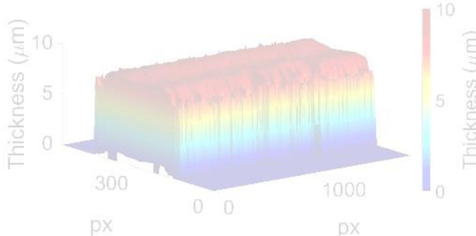

5 3D Quantification of Line Morphology

2 Sensor-Instrumented Experimental Setup

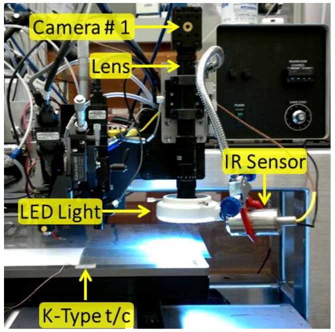

4 Computational Fluid Dynamics Modeling

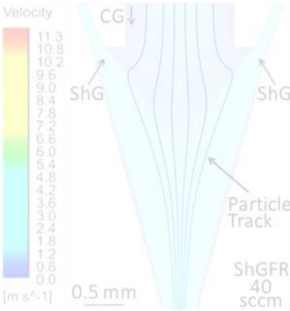

6 *In Situ* Estimation of Line Resistance

Sensor-Instrumented Setup

The AJP setup is supported by high-resolution CCD cameras, allowing for *in situ* image acquisition.

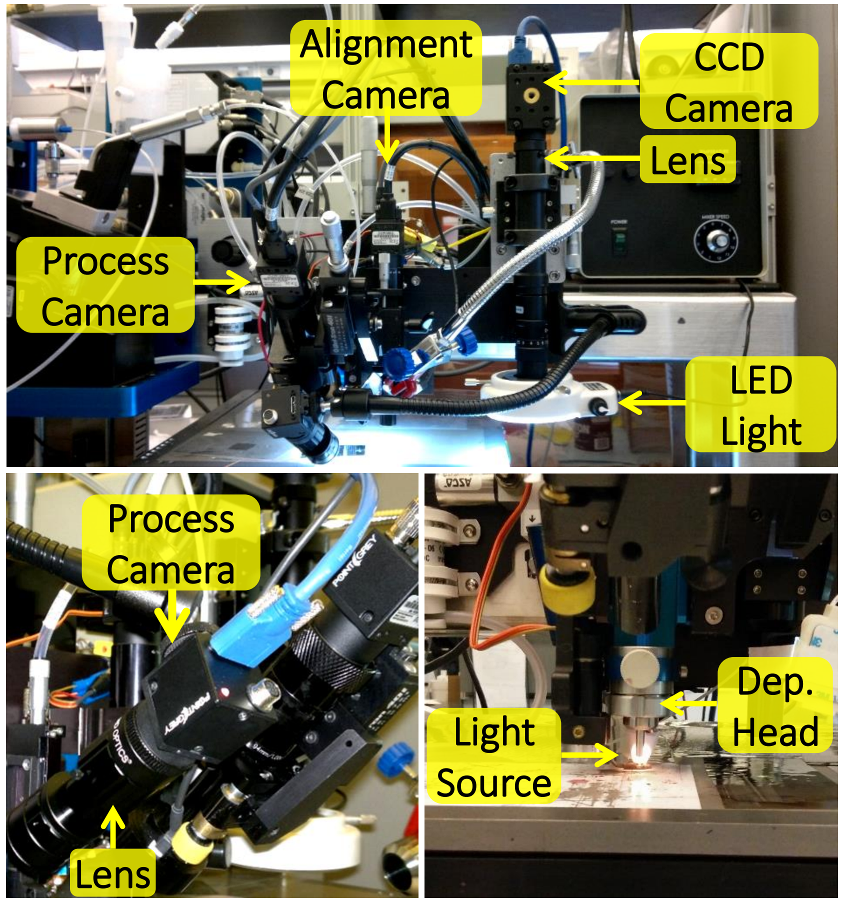

Salary, R., *et al.*, 2016, Journal of Manufacturing Science and Engineering, 139(2), p. 021015.

Using the in-line imaging system, images are acquired from the traces of a device right after deposition.

Outline

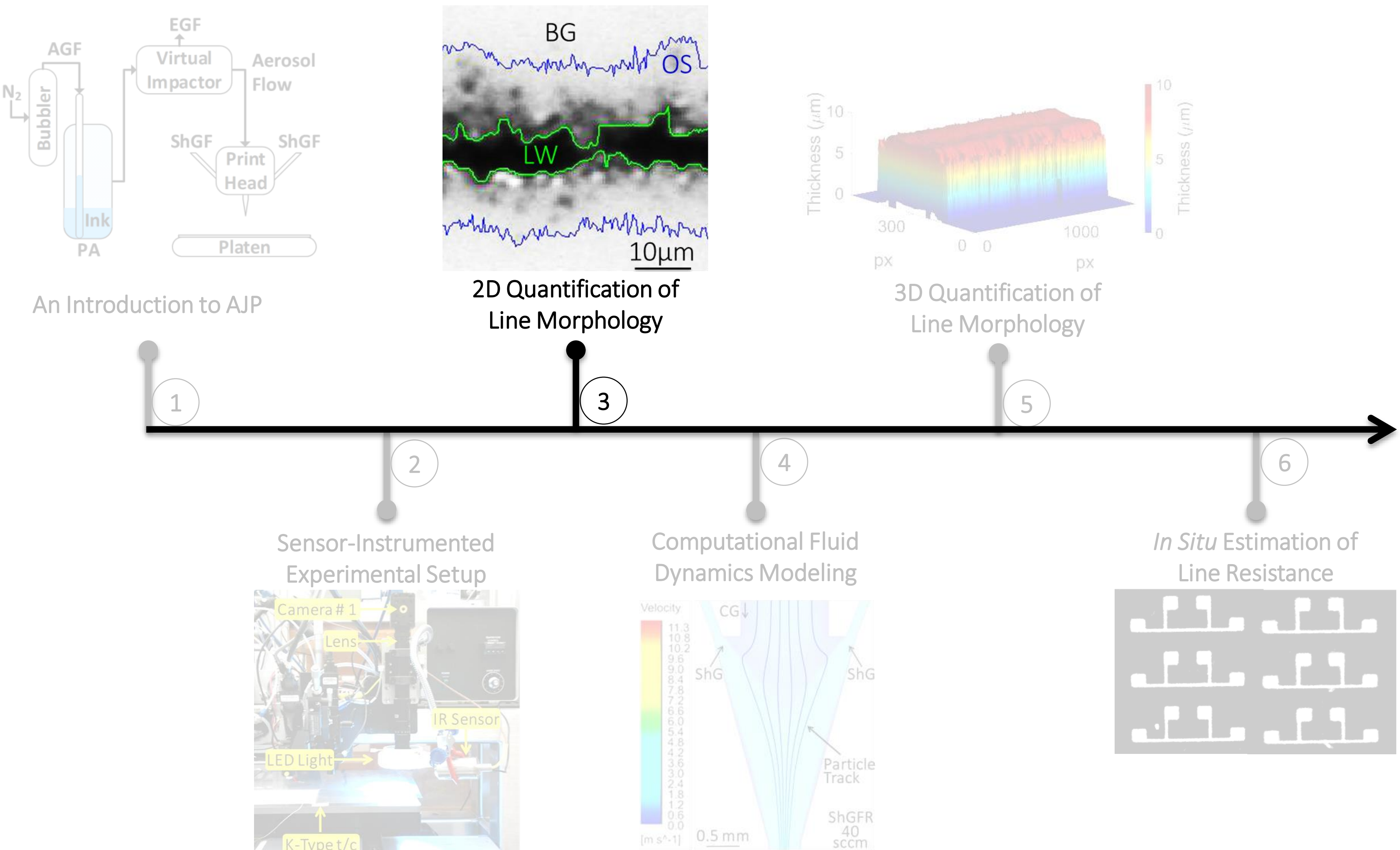
N2
Bubbler
AGF
EGF
Virtual Impactor
Aerosol Flow
ShGF
Print Head
ShGF
Ink
PA
Platen
An Introduction to AJP
1
BG
OS
LW
10µm
2D Quantification of Line Morphology
3
Thickness (µm)
300
1000
px
px
3D Quantification of Line Morphology
5
2
Sensor-Instrumented Experimental Setup
Camera # 1
Lens
IR Sensor
LED Light
K-Type t/c
4
Computational Fluid Dynamics Modeling
Velocity
CG
ShG
ShG
Particle Track
0.5 mm
ShGFR 40 sccm
6
In Situ Estimation of Line Resistance

Quantification of 2D Features of Line Morphology

Image-based quantifiers are introduced to capture several aspects of line morphology.

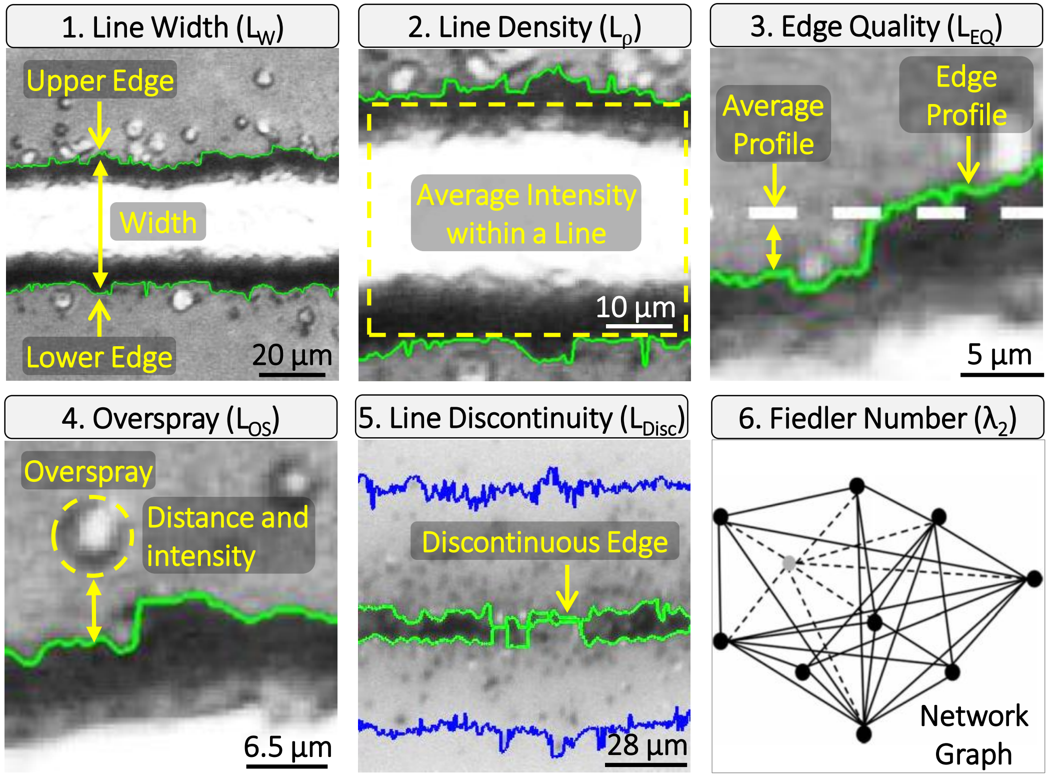

Salary, R., *et al.*, 2016, Journal of Manufacturing Science and Engineering, 139(2), p. 021015.
P. Rao, *et al.*, 2015, IIE Transactions, *Quality and Reliability Engineering*, 47(10), pp. 1-24.

Fiedler number, a graph-theoretic quantifier, is used as a measure of surface morphology.

Several aspects of line morphology are captured, based on the proposed image-based quantifiers.

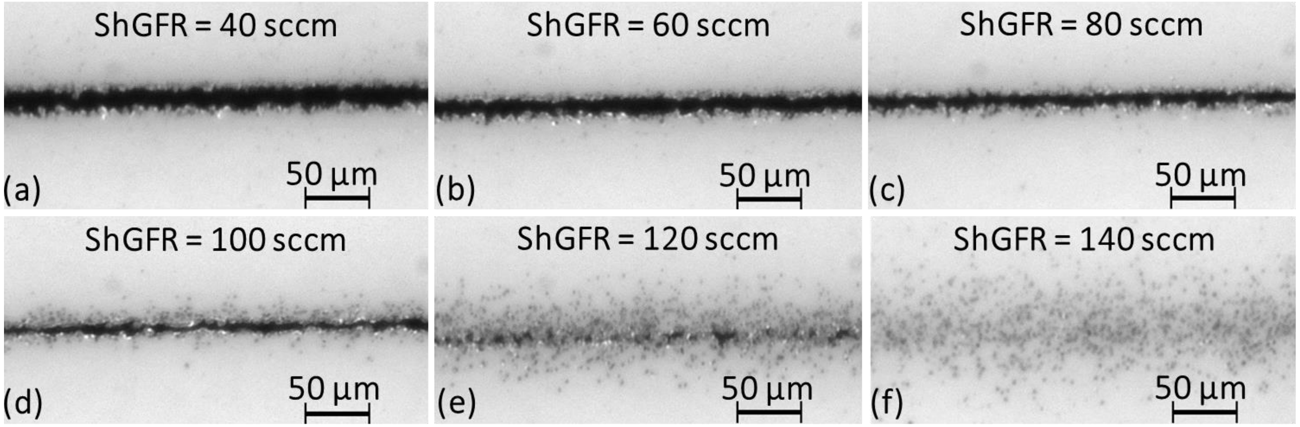

Salary, R., *et al*., 2016, Journal of Manufacturing Science and Engineering, 139(2), p. 021015.

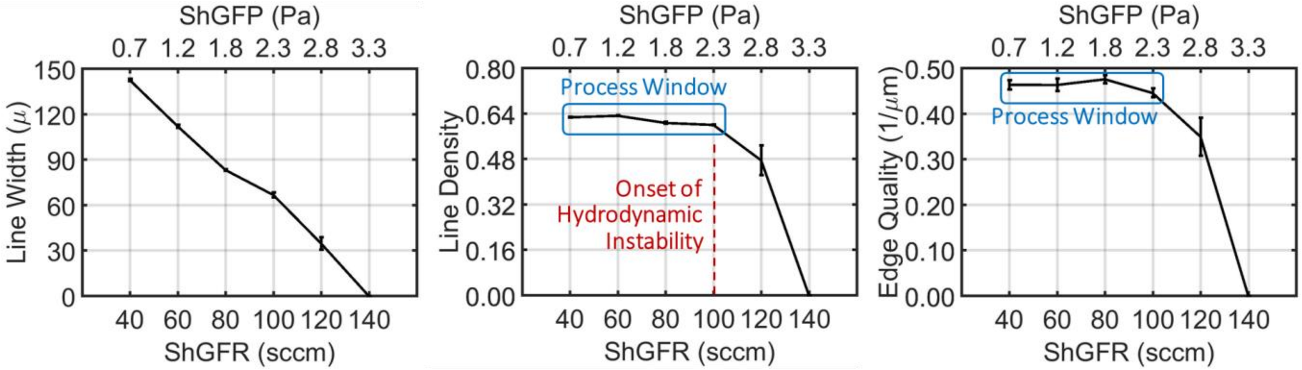

Salary, R., *et al*., 2016, Journal of Manufacturing Science and Engineering, 139(2), p. 021015.

In situ quantification of line morphology allows for process monitoring and closed-loop control in AJP.

Quantification of 2D Features – Case Study

Several aspects of line morphology are captured, based on the proposed image-based quantifiers.

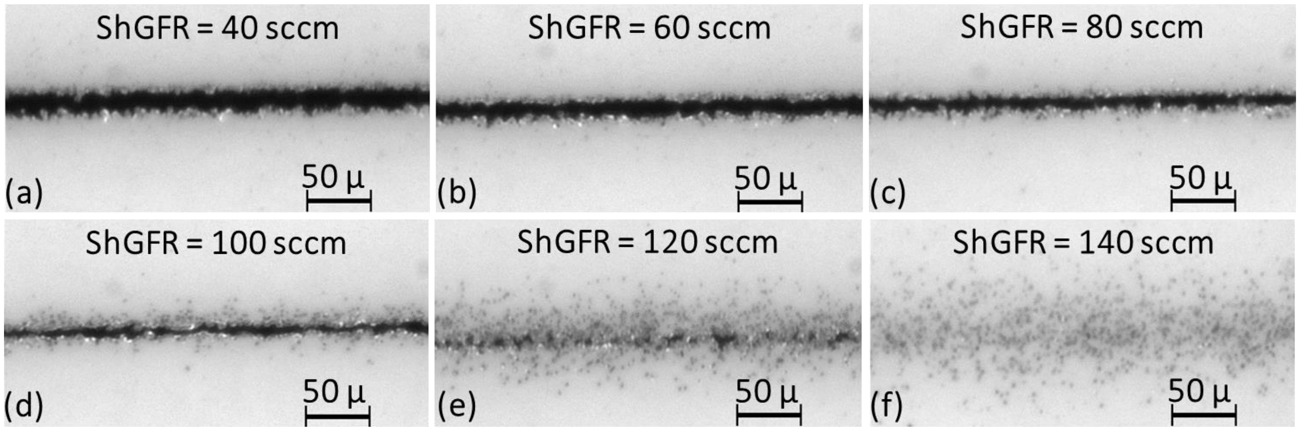

Salary, R., *et al.*, 2016, Journal of Manufacturing Science and Engineering, 139(2), p. 021015.

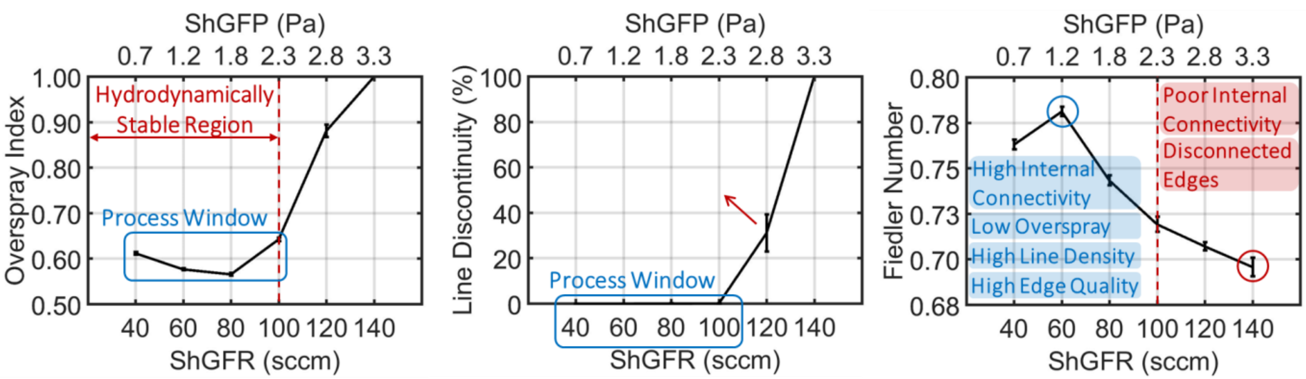

Salary, R., *et al.*, 2016, Journal of Manufacturing Science and Engineering, 139(2), p. 021015.

In situ quantification of line morphology allows for process monitoring and closed-loop control in AJP.

Outline

An Introduction to AJP

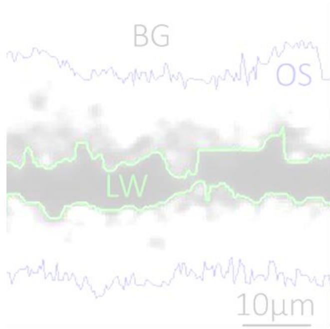

2D Quantification of Line Morphology

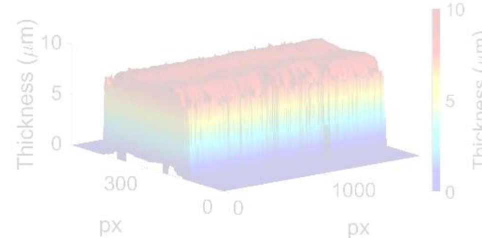

3D Quantification of Line Morphology

1
2
3
4
5
6

Sensor-Instrumented Experimental Setup

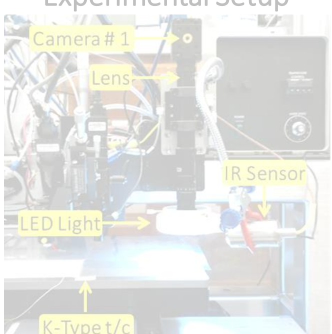

Computational Fluid Dynamics Modeling

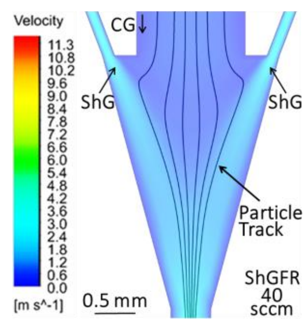

In Situ Estimation of Line Resistance

Computational Fluid Dynamics (CFD) Modeling

The deposition head was modeled, based on a patent and X-ray imaging.

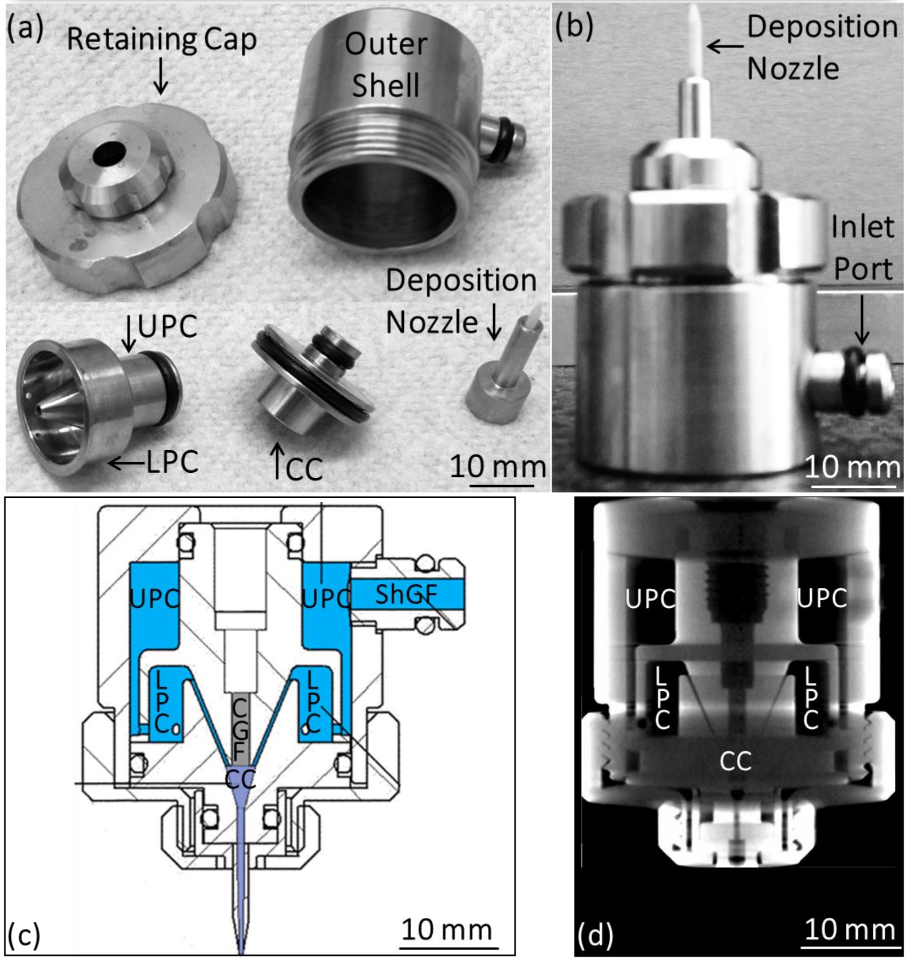

King, B. H., Patent: US8640975 B2., Feburary 4, 2014.
Salary, R., *et al.*, 2016, Journal of Manufacturing Science and Engineering, 139(2), p. 021015.

The deposition head was CT-scanned to measure the internal structure accurately.

Computational Fluid Dynamics (CFD) Modeling

Discrete-Phase Modeling

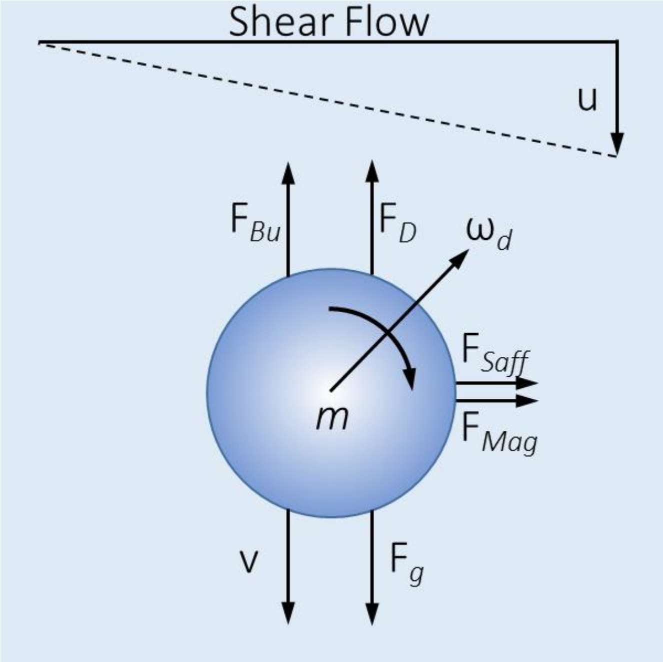

Salary, R., *et al.*, 2016, ASME-JMSE, 139(2), p. 021015.

$$\sum \mathbf{F} = \mathbf{F}_D + \mathbf{F}_{Basset} + \mathbf{F}_{VM} + \mathbf{F}_{PG} + \mathbf{F}_g + \mathbf{F}_{Bu} + \mathbf{F}_{Saff} + \mathbf{F}_{Mag}$$

Boundary Conditions

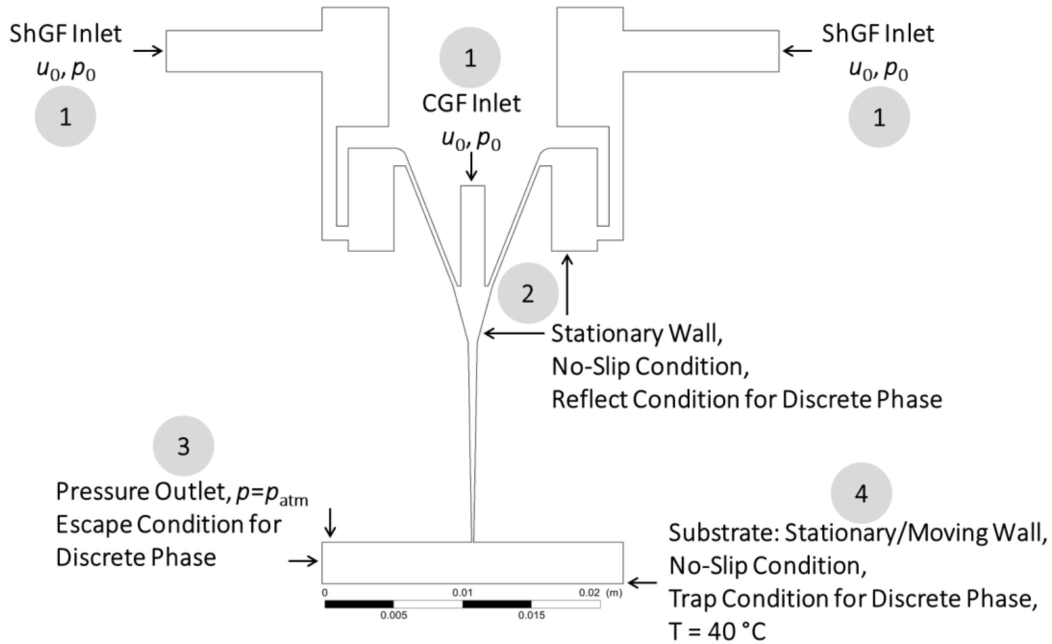

Salary, R., *et al.*, 2016, Journal of Manufacturing Science and Engineering, 139(2), p. 021015.

Only the drag force and Saffman lift force are significant.

Hoey, J. M., *et al.*, Hindawi Journal of Nanotechnology, 2012.
Akhatov, I., *et al.*, Microfluidics and Nanofluidics, **5**(2), pp. 215-224, 2008.
Crowe, C. T., *et al.*, Multiphase Flows with Droplets and Particles, 2nd Ed., CRC Press, Boca Raton, FL, USA, 2011.
Marshall, J., Journal of Computational Physics, **228**(5), pp. 1541-1561, 2009.

Computational Fluid Dynamics (CFD) Modeling

At high ShGFRs (≥ 100 sccm), pressure builds up in the head, leading to uneven aerosol deposition and poor line quality.

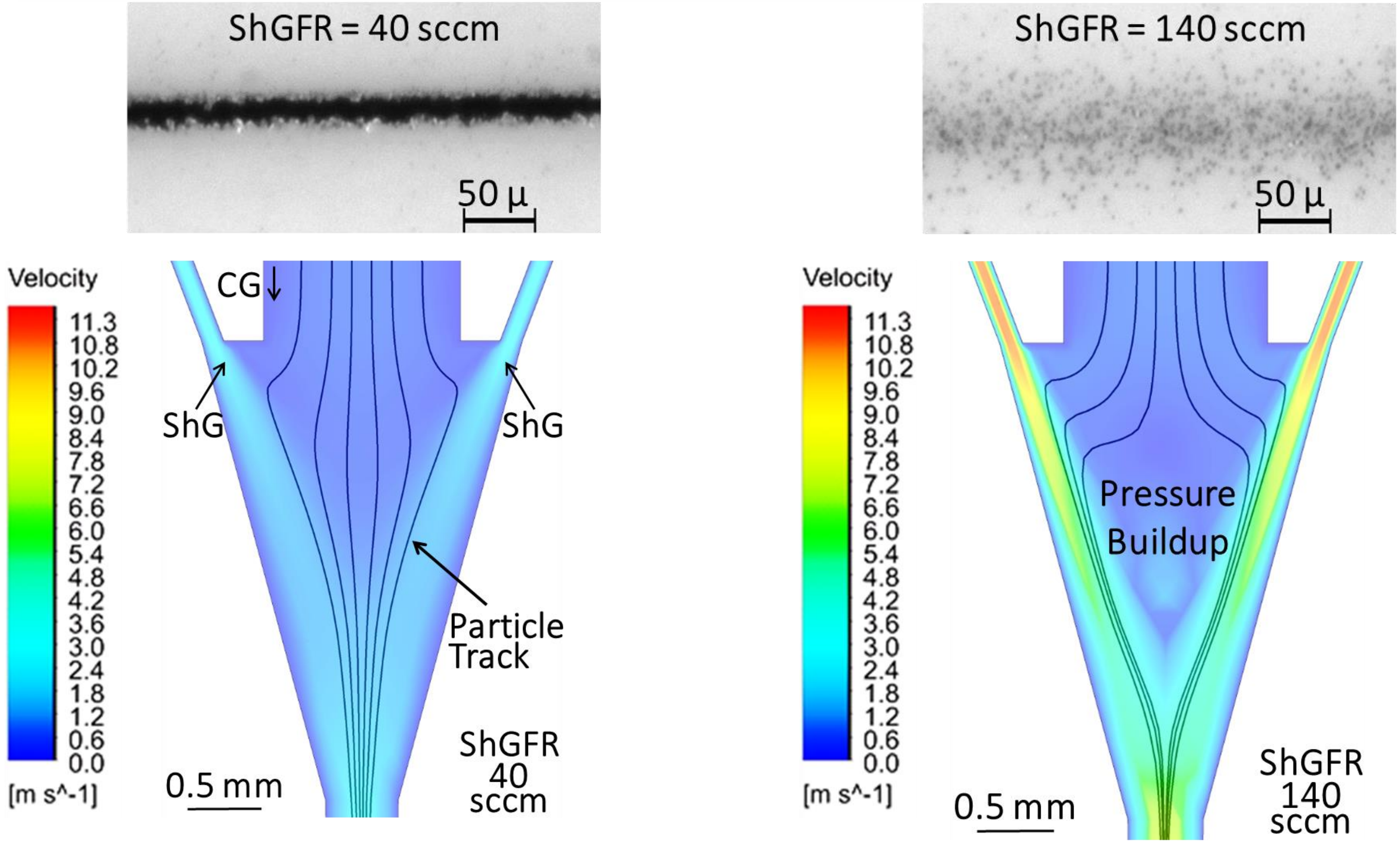

Salary, R., *et al.*, 2016, Journal of Manufacturing Science and Engineering, 139(2), p. 021015.

Collimation of the aerosol flow is limited due to the pressure buildup in the deposition head.

CFD Model Validation with Experimental Results

The aerosol deposition profile becomes narrower when the ShGFR increases, as observed experimentally.

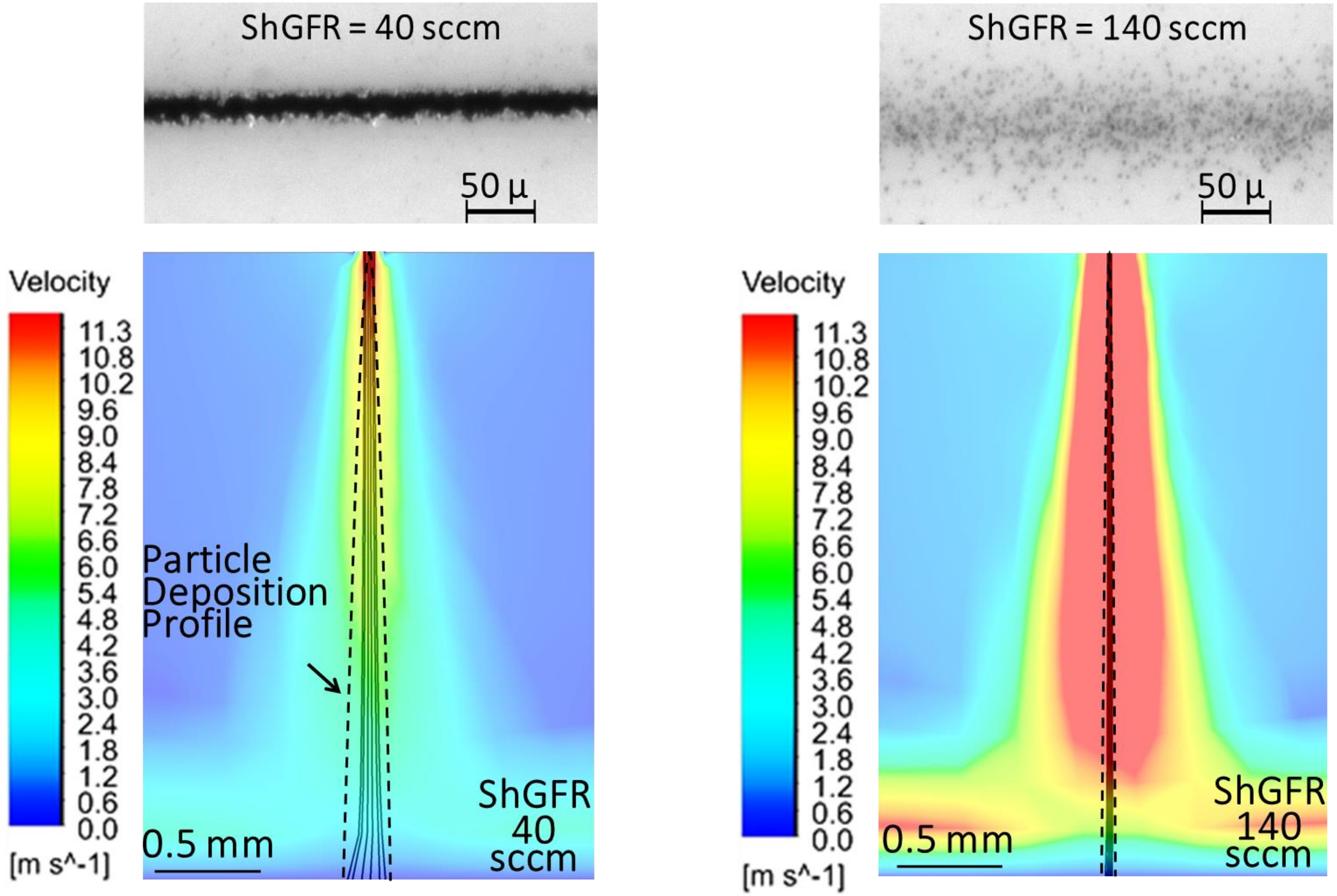

Salary, R., *et al*., 2016, Journal of Manufacturing Science and Engineering, 139(2), p. 021015.

More focused aerosol deposition is obtained at high ShGFRs.

CFD Model Validation with Experimental Results

The pressure buildup in the combination chamber becomes significant at the ShGFR of 80 sccm onwards.

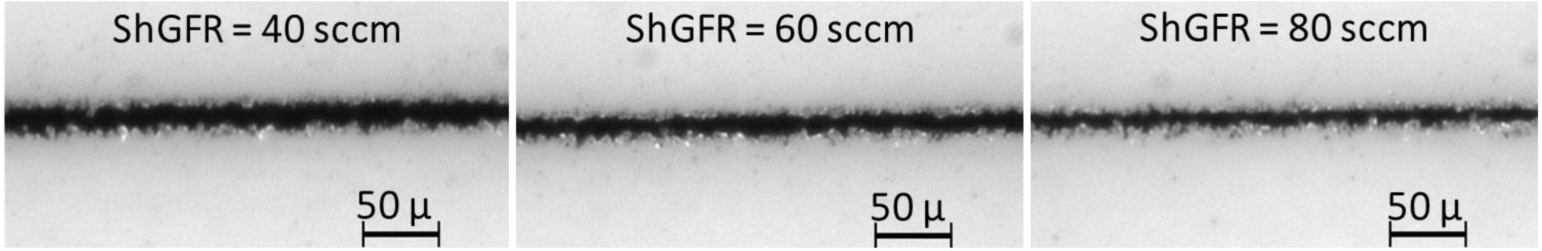

Salary, R., *et al.*, 2016, Journal of Manufacturing Science and Engineering, 139(2), p. 021015.

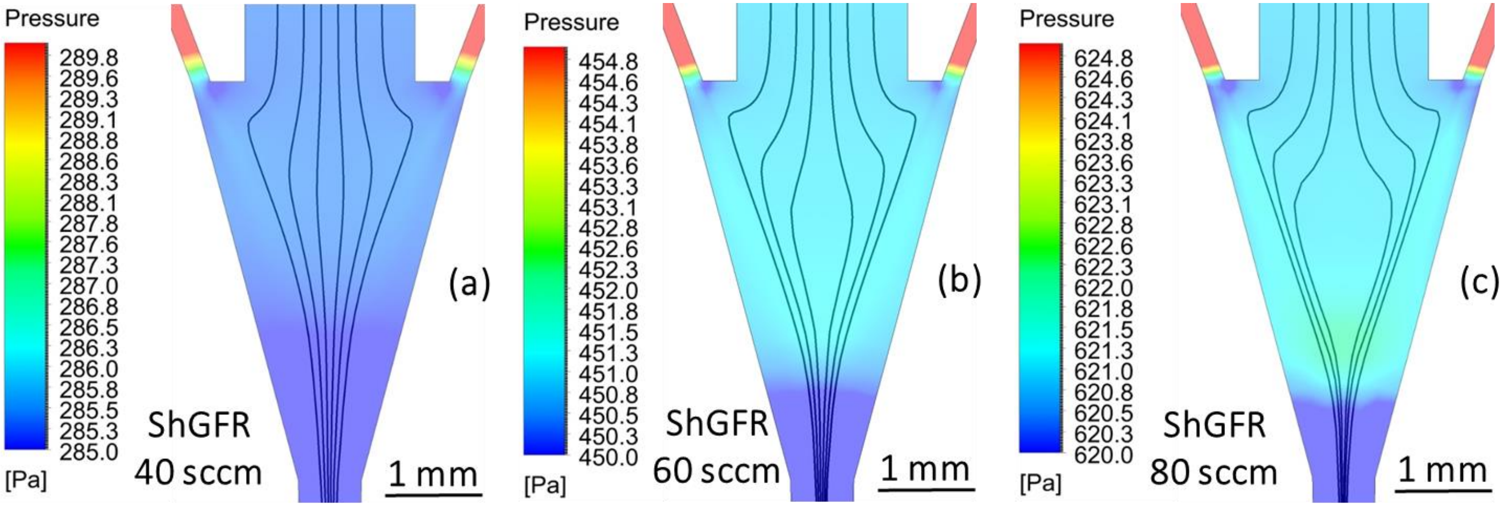

Salary, R., *et al.*, 2016, Journal of Manufacturing Science and Engineering, 139(2), p. 021015.

The maximum pressure limit is approximately 622 Pa.

CFD Model Validation with Experimental Results

The pressure buildup in the combination chamber becomes significant at the ShGFR of 80 sccm onwards.

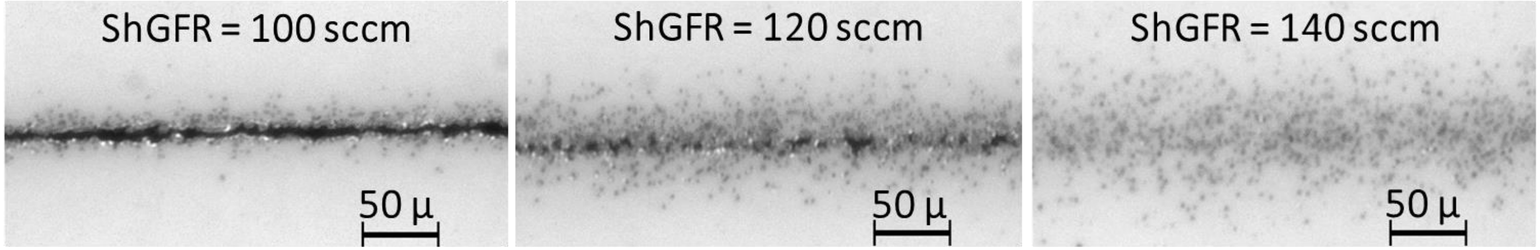

Salary, R., *et al.*, 2016, Journal of Manufacturing Science and Engineering, 139(2), p. 021015.

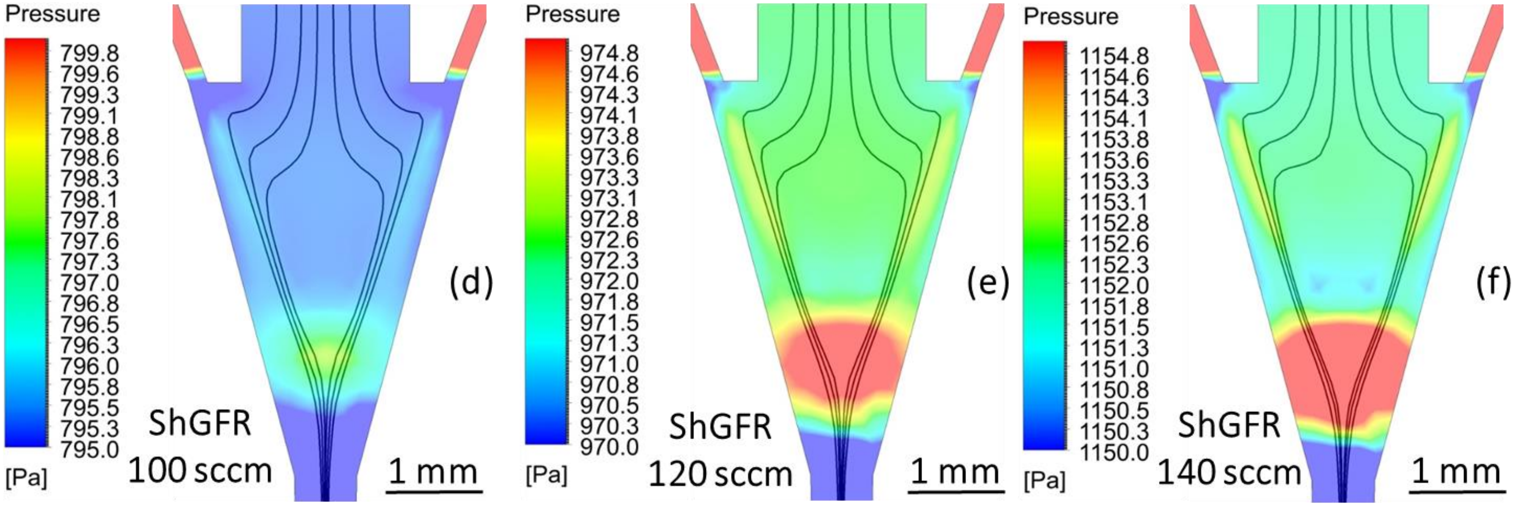

Salary, R., *et al.*, 2016, Journal of Manufacturing Science and Engineering, 139(2), p. 021015.

The maximum pressure limit is approximately 622 Pa.

An Introduction to AJP

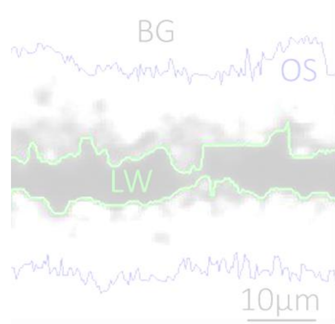

2D Quantification of Line Morphology

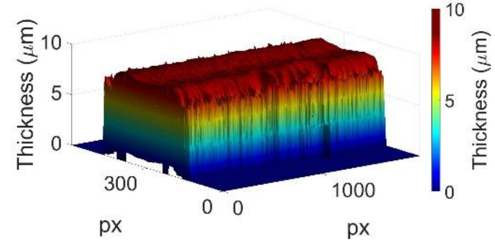

3D Quantification of Line Morphology

1

2

3

4

5

6

Sensor-Instrumented Experimental Setup

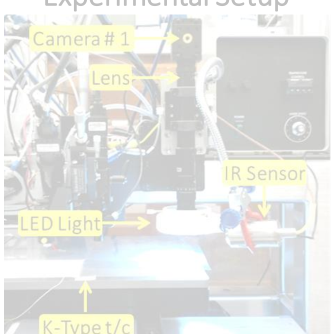

Computational Fluid Dynamics Modeling

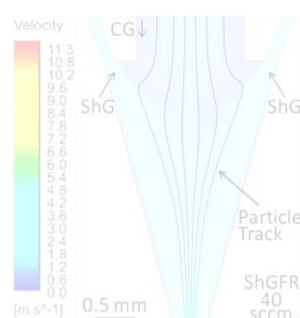

In Situ Estimation of Line Resistance

Quantification of 3D Features of Line Morphology

Line topology can be recovered, given an image, illumination direction, and surface reflectivity.

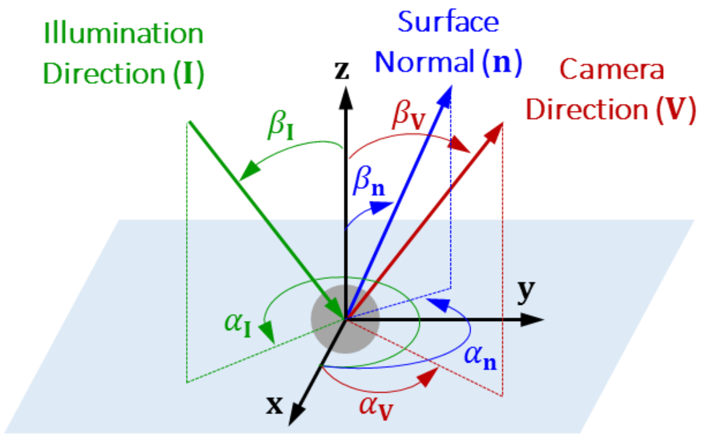

Salary, R., *et al.*, 2017, Journal of Manufacturing Science and Engineering, 139(10), p. 101010.

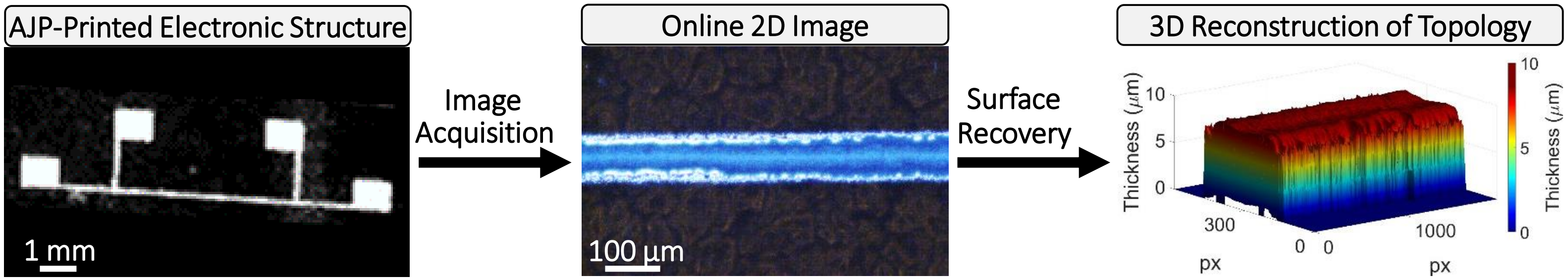

Salary, R., *et al.*, 2017, Journal of Manufacturing Science and Engineering, 139(10), p. 101010.

Recovery of line topology allows for *in situ* estimation of 3D characteristics, such as thickness, CSA, and surface roughness.

Quantification of 3D Features of Line Morphology

Surface reflectance mathematically corresponds to image irradiance, and constitutes the basis for all SfS methods.

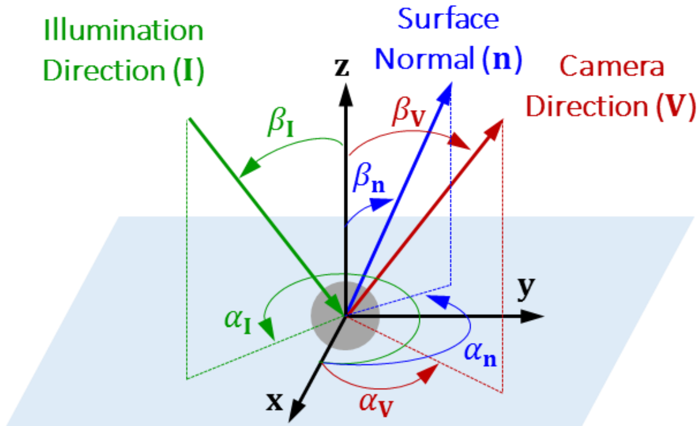

Salary, R., *et al.*, 2017, Journal of Manufacturing Science and Engineering, 139(10), p. 101010.

$$\mathbf{I} = [\sin\alpha_\mathbf{I}\cos\beta_\mathbf{I}, \sin\alpha_\mathbf{I}\sin\beta_\mathbf{I}, \cos\alpha_\mathbf{I}]^T$$

$$\mathbf{n} = \frac{[-p, -q, 1]^T}{\sqrt{1+p^2+q^2}}$$

$$p = \frac{\partial Z_{(x,y)}}{\partial x} \qquad q = \frac{\partial Z_{(x,y)}}{\partial y}$$

$$E(x,y) = \frac{\rho \mathbf{I}^T[-p, -q, 1]^T}{\sqrt{1+p^2+q^2}}$$

Salary, R., *et al.*, 2017, Journal of Manufacturing Science and Engineering, 139(10), p. 101010.
Elhabian, S. Y., 2008, Computer Vision and Image Processing (CVIP) Laboratory, University of Louisville, Louisville, KY, USA.

The SfS problem is intrinsically underdetermined. Certain assumptions are needed to establish a well-posed problem.

Quantification of 3D Features of Line Morphology

Five fundamental assumptions are made to convert the SfS problem to a well-posed, balanced problem.

(1) The camera has orthographic projection.
(2) The z-axis of the camera represents the optical axis.
(3) The surface is diffuse or Lambertian.
(4) The surface is not self-shadowing.
(5) Illumination direction and surface albedo are constant.

Salary, R., *et al*., 2017, Journal of Manufacturing Science and Engineering, 139(10), p. 101010.
Elhabian, S. Y., 2008, Computer Vision and Image Processing (CVIP) Laboratory, University of Louisville, Louisville, KY, USA.

Depending on the method of choice, additional assumptions may be needed to further simply the problem.

Literature Review

There are four broad classes of SfS approaches: Minimization, Propagation, Local, and Linear.

Elhabian, S. Y., 2008, Computer Vision and Image Processing (CVIP) Laboratory, University of Louisville, Louisville, KY, USA.
Zhang, R., *et al.*, 1999, IEEE Transactions on Pattern Analysis and Machine Intelligence, **21**(8), pp. 690-706.

Minimization

Horn, Chellappa, Szeliski, Maydan, Kuo, Bobick, and Yang

Horn, B. K., *et al.*, 1989, MIT Press, Cambridge, MA, USA.
Zheng, Q., *et al.*, 1991, IEEE CVPR '91, Maui, HI, USA, pp. 540-545.
Szeliski, R., 1991, CVGIP: Image Understanding, **53**(2), pp. 129-153.
Malik, J., *et al.*, 1989, IEEE Transactions on Pattern Analysis and Machine Intelligence, **11**(6), pp. 555-566.
Lee, K. M., *et al.*, 1993, IEEE Transactions on Pattern Analysis and Machine Intelligence, **15**(8), pp. 815-822.
Leclerc, Y. G., *et al.*, 1991, IEEE CVPR'91, pp. 552-558.
Vega, O. E., *et al.*, 1993, IEEE Transactions on Pattern Analysis and Machine Intelligence, **15**(6), pp. 592-597.

Propagation

Tourin, Oliensis, and Bruckstein

Rouy, E., *et al.*, 1992, SIAM Journal on Numerical Analysis, **29**(3), pp. 867-884.
Dupuis, P., *et al.*, 1992, IEEE CVPR'92, pp. 453-458.
Kimmel, R., *et al.*, 1992, Technion-Israel Institute of Technology, Report 9209.

Local

Rosenfeld and Pentland

Lee, C.-H., *et al.*, 1985, artificial Intelligence, **26**(2), pp. 125-143.

Linear

Pentland and Shah

Pentland, A., 1989, Spatial vision, **4**(2), pp. 165-182.
Ping-Sing, T., *et al.*, 1994, Image and Vision computing, **12**(8), pp. 487-498.

The local and propagation approaches are not used due to their underlying computational complexity and delay.

Salary, R., *et al.*, 2017, Journal of Manufacturing Science and Engineering, 139(10), p. 101010.
Elhabian, S. Y., 2008, Computer Vision and Image Processing (CVIP) Laboratory, University of Louisville, Louisville, KY, USA.

Quantification of 3D Features of Line Morphology

The performance of the three SfS methods is assessed using synthetic and real images.

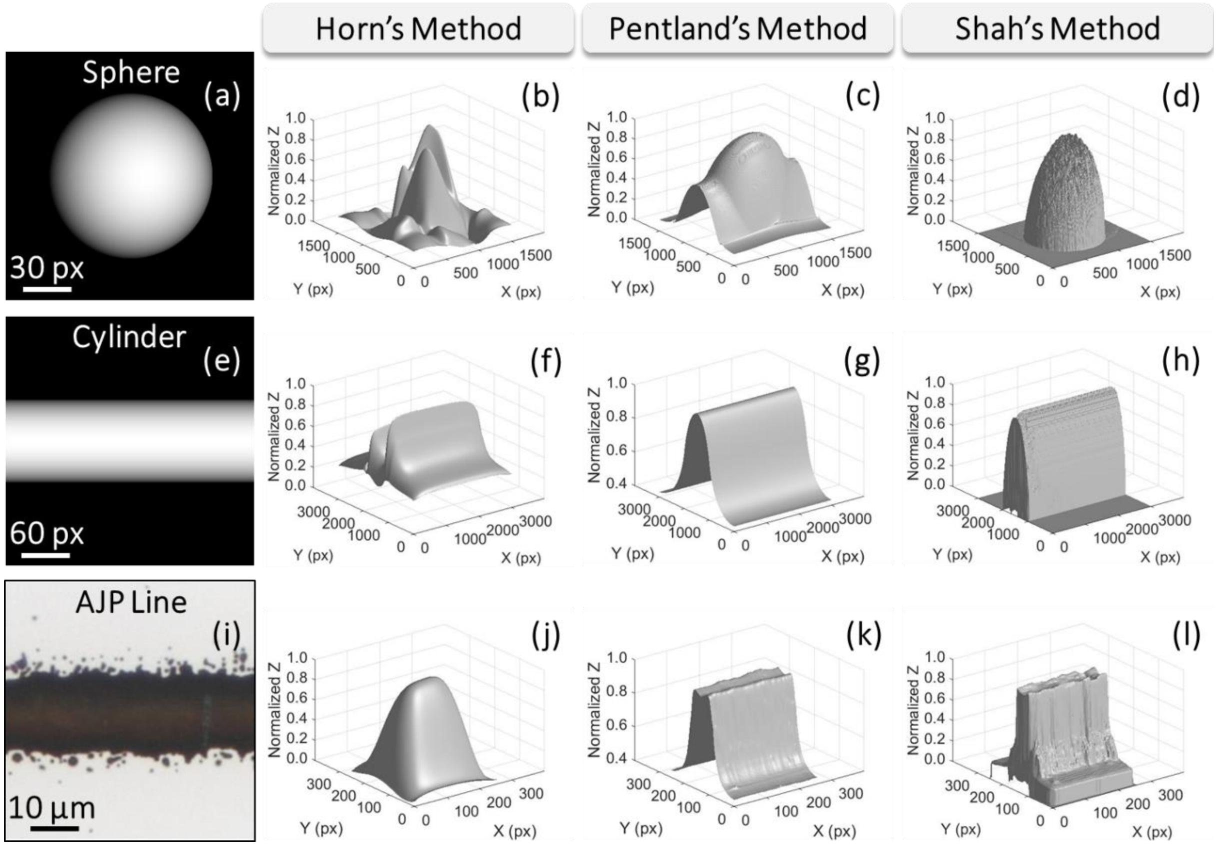

Salary, R., *et al.*, 2017, Journal of Manufacturing Science and Engineering, 139(10), p. 101010.

The Shah's method has the highest accuracy and hence, is used for reconstructing the 3D profile of AJP lines.

Quantification of 3D Features – Case Study

Having recovered the 3D profile of a trace, the critical features of the trace topology can be quantified.

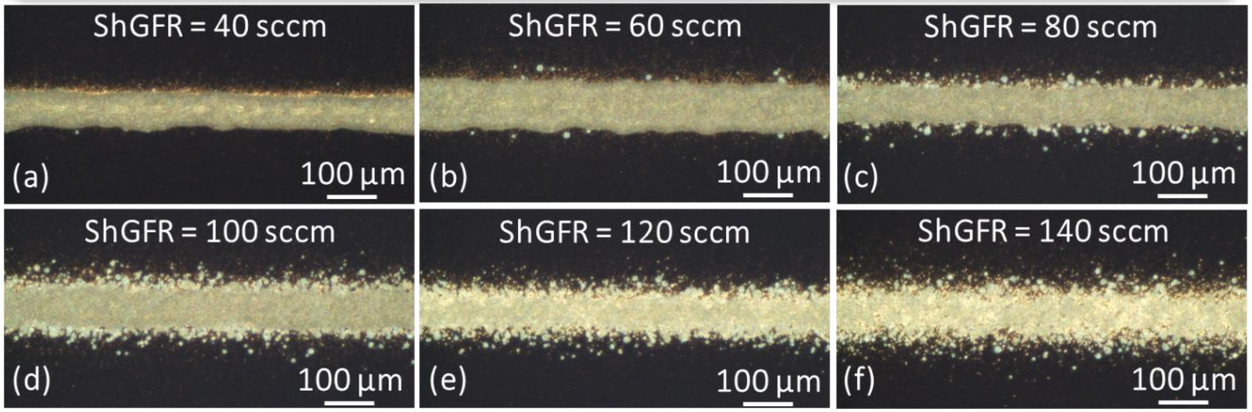

Salary, R., *et al.*, 2017, Journal of Manufacturing Science and Engineering, 139(10), p. 101010.

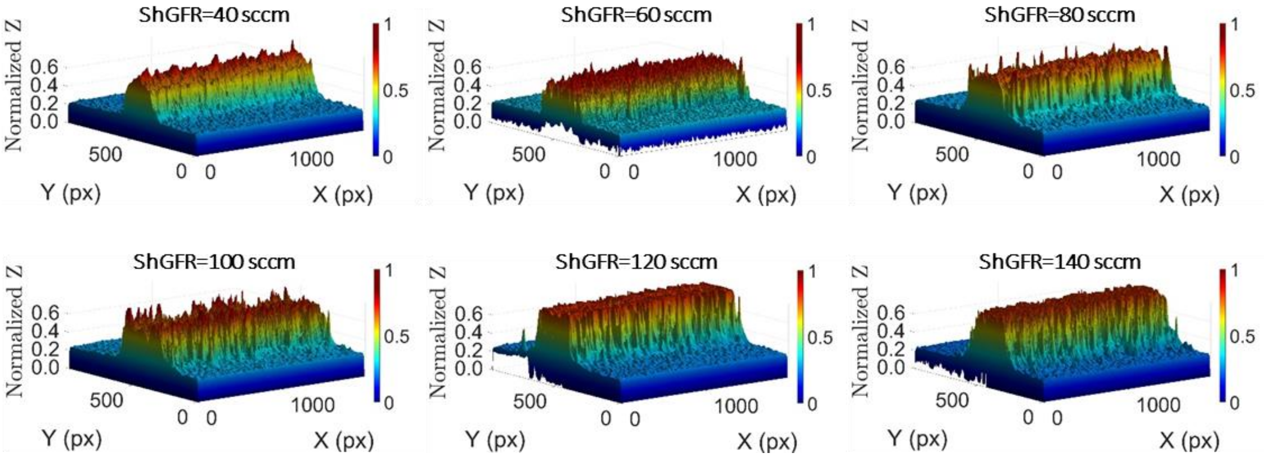

Salary, R., *et al.*, *ASME J. Manuf. Sci. Eng.*, 139(10): 101010-101010-13, 2017.

Recovery and quantification of line topology pave the way for *in situ* monitoring of device functional properties.

Outline

1 An Introduction to AJP

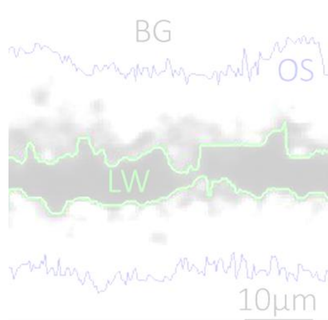

3 2D Quantification of Line Morphology

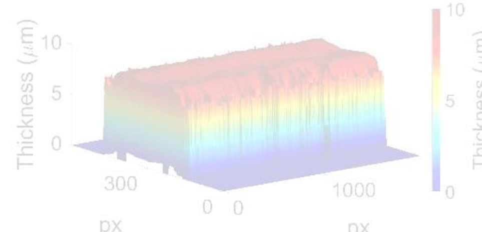

5 3D Quantification of Line Morphology

2 Sensor-Instrumented Experimental Setup

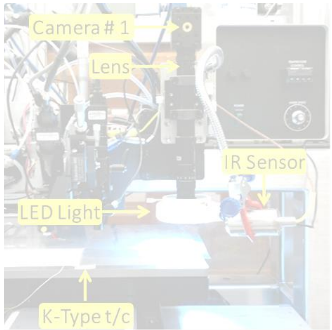

4 Computational Fluid Dynamics Modeling

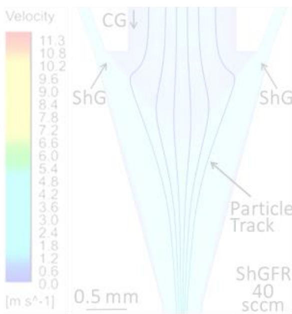

6 *In Situ* Estimation of Line Resistance

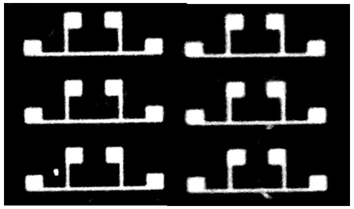

Development of a MISO Classification Model

Sparse representation for classification (SRC) is a supervised learning technique, requiring *a priori* labels.

SRC formulates an underdetermined system of linear equations with N unknowns/samples and m equations/features ($N > m$).

$$Y = A\beta + \varepsilon$$

$Y \in \mathbb{R}^{m\times 1}$ | $\beta \in \mathbb{R}^{N\times 1}$ | $A \in \mathbb{R}^{m\times N}$ | ε

A New Sensor Signal | Unknown Vector of Coefficients | Design Matrix | Error

Assuming $\boldsymbol{\beta}$ is sparse

$$\min \|\beta\|_0 \quad s.t.: \ f(\underbrace{Y - A\beta}_{\text{Residual}}) \le \delta$$

Threshold

Convex Optimization

$$\min \|\beta\|_1 \quad s.t.: \ \|Y - A\beta\|_2^2 \le \delta$$

Salary, R., *et al.*, ASME-MSEC 2018, Texas A&M University, College Station, TX, USA, June 18-22, 2018.

The objective is to estimate β, and thus determine the class of a new sensor signal (Y).

Development of a MISO Classification Model

A novel optimization problem is formulated, based on LASSO, Elastic Net, and Ridge Regression.

Sum of Squared Errors (SSE)

$$\hat{\beta} = \underset{\beta}{\operatorname{argmin}} \left(\overbrace{\|Y - A\beta\|_2^2}^{\text{Sum of Squared Errors (SSE)}} + \underbrace{\lambda}_{\text{Regularization Parameter}} \left(\frac{1 - \alpha}{2} \underbrace{\|\beta\|_2^2}_{\text{Variance of Coefficients}} + \alpha \underbrace{\|\beta\|_1}_{\text{Number of Coefficients}} \right) \right)$$

Weighting Parameter

Regularization Parameter

Variance of Coefficients

Number of Coefficients

Salary, R., *et al.*, ASME-MSEC 2018, Texas A&M University, College Station, TX, USA, June 18-22, 2018.

$$c = \underset{c}{\operatorname{argmin}} \left(A \underbrace{\delta_c}_{\text{Sparsifying Operator}} (\hat{\beta}) - Y \right)$$

Sparsifying Operator

If $\boldsymbol{\alpha} \approx \mathbf{0}$: **Ridge Regression** ($\ell_2$ minimization);
If $\boldsymbol{\alpha} = \mathbf{1}$: **LASSO** ($\ell_1$ minimization)
If $\mathbf{0} < \boldsymbol{\alpha} < \mathbf{1}$: **Elastic Net** ($\ell_1$ and ℓ_2 minimization).

Development of a MISO Classification Model

An classification space is mapped using a heuristic method, giving the optimal values of λ and α.

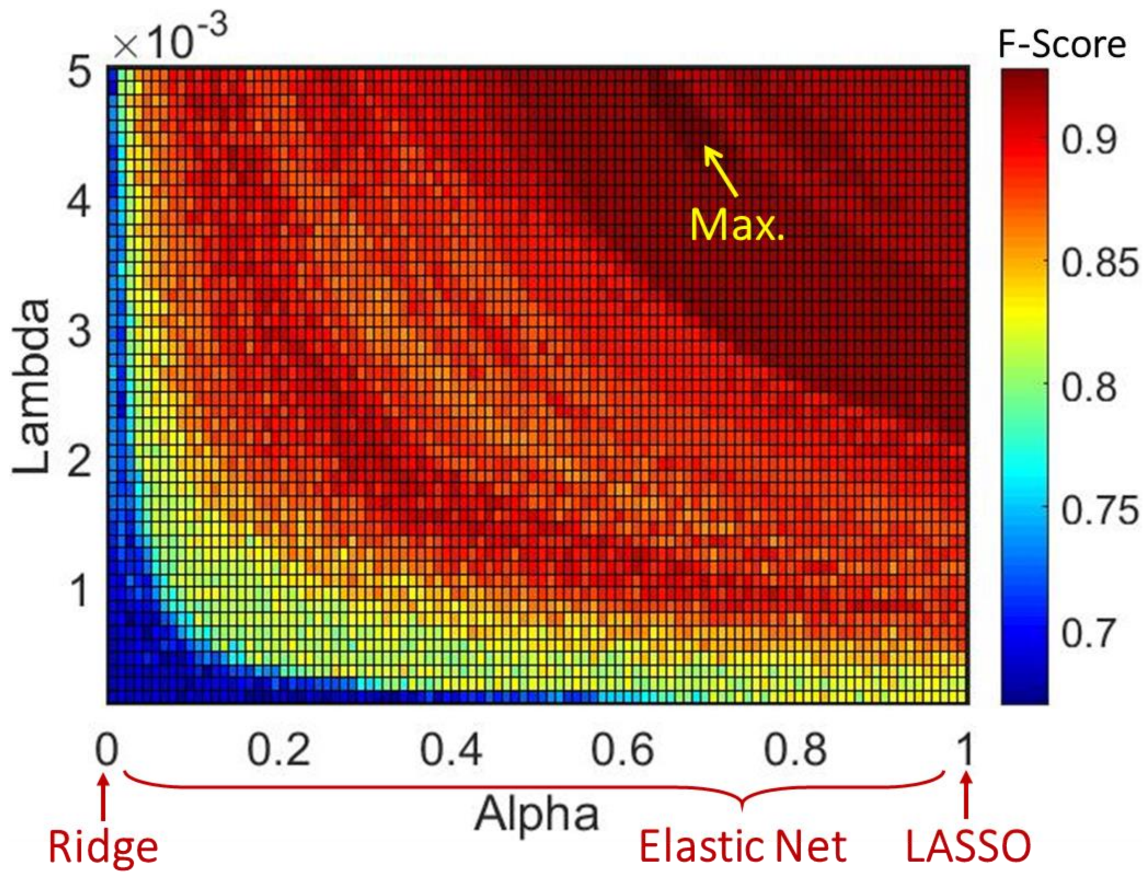

Salary, R., *et al.*, ASME-MSEC 2018, Texas A&M University, College Station, TX, USA, June 18-22, 2018.

60% of the data is dedicated to training, 30% to validation (parameter optimization), and 10% to testing.

Development of a MISO Classification Model

Electronic traces were printed three times for each treatment combination of the experimental design.

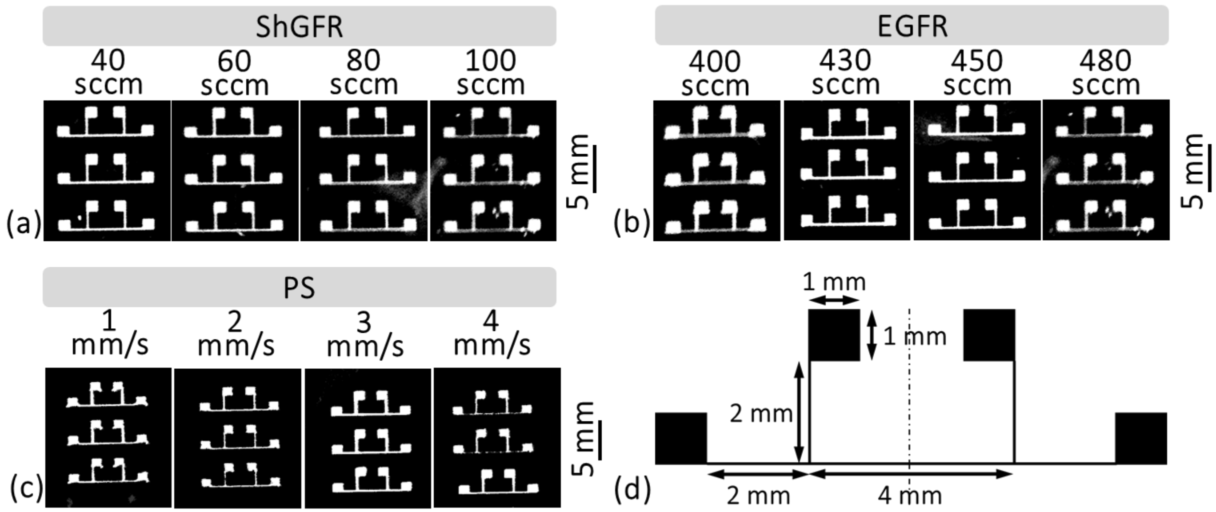

Salary, R., *et al.*, ASME-MSEC 2018, Texas A&M University, College Station, TX, USA, June 18-22, 2018.

These structures allow for 4-point probe measurements of line resistance, and definition of *a priori* classification labels.

Development of a MISO Classification Model

Using the CCD camera, online images were acquired from each trace, and subsequently processed.

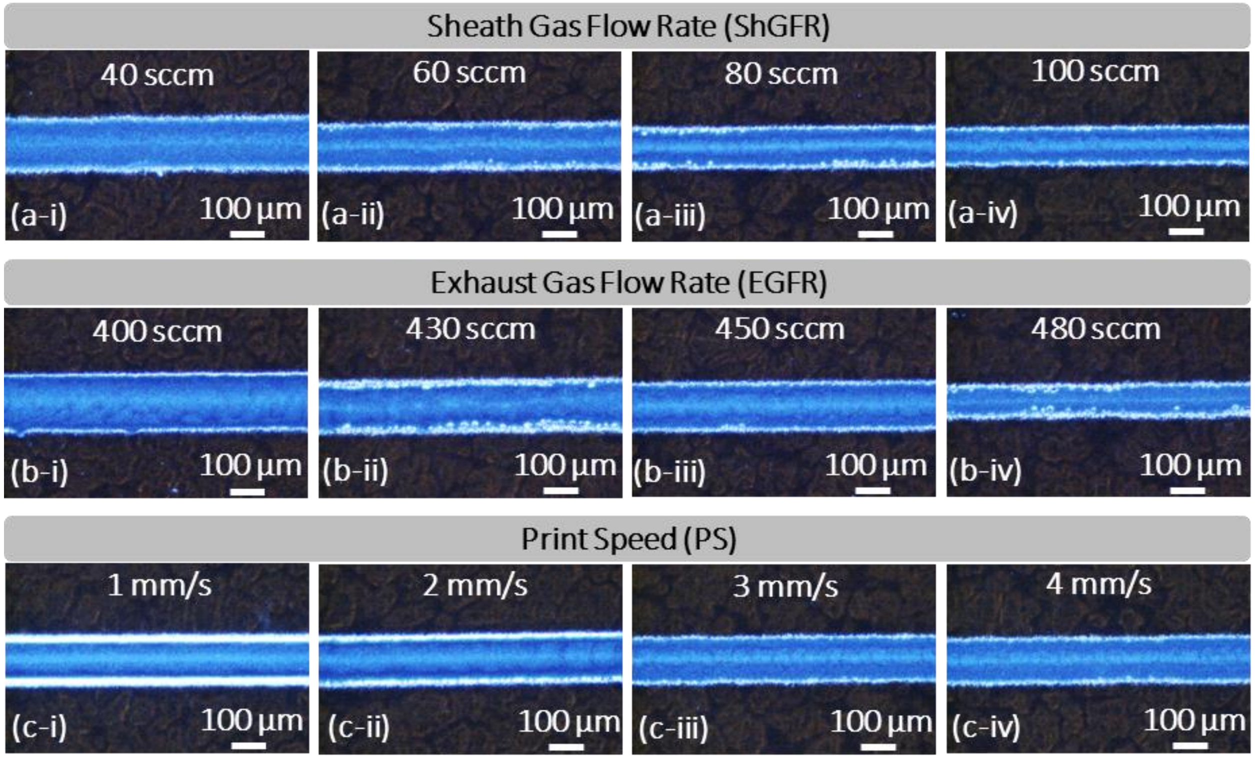

Salary, R., *et al*., ASME-MSEC 2018, Texas A&M University, College Station, TX, USA, June 18-22, 2018.

3D features were additionally quantified after recovery of the line topology using SfS image analysis.

Development of a MISO Classification Model

In situ reconstruction of the line topology for near real-time quantification of the CSA and other 3D features.

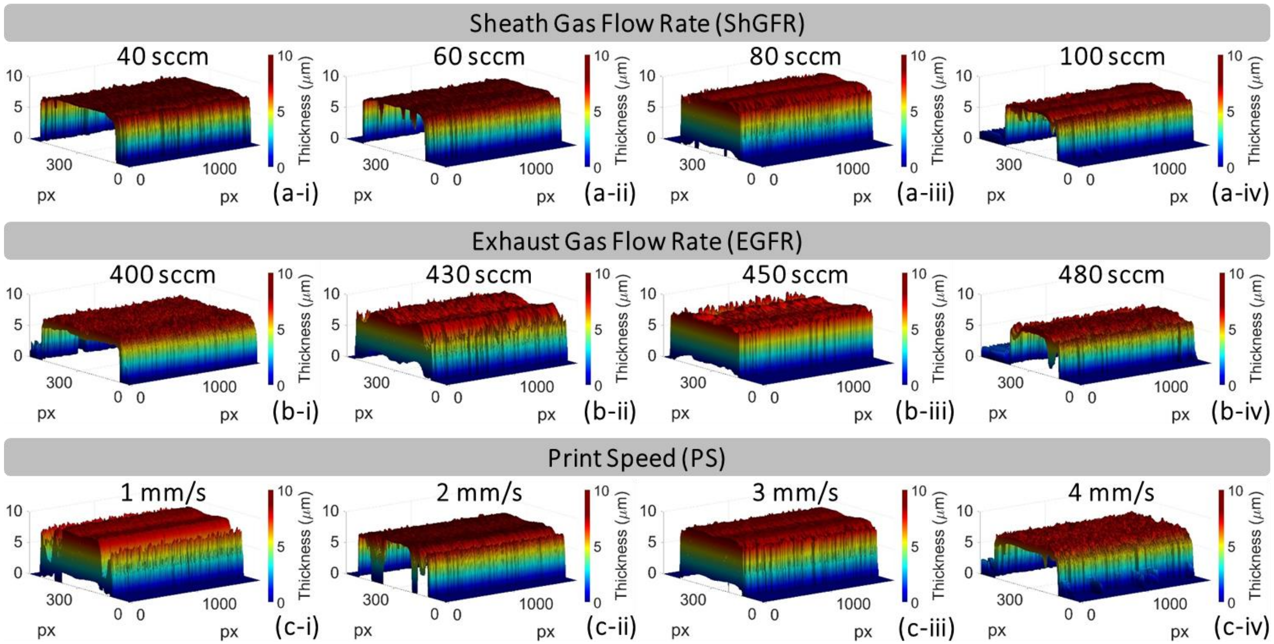

Salary, R., *et al.*, ASME-MSEC 2018, Texas A&M University, College Station, TX, USA, June 18-22, 2018.

In total, around 30 morphology features were extracted from each image, fed as inputs to the machine learning model.

Development of a MISO Classification Model

The classification performance implies the line resistance can be accurately estimated online.

Classification Results		Predicted Condition		
Optimal Method: LASSO		Class 1	Class 2	Class 3
True Condition	Class 1	1	0	0
	Class 2	0	0.92	0.08
	Class 3	0	0	1
Classification Measures	Recall	1	0.92	1
	Precision	1	1	0.92
	False Alarm	0	0	0
	Specificity	1	1	1
Optimization	λ (Opt)		0.0041	
	α (Opt)		1	
Performance Evaluation	F-Score		0.97	

Salary, R., *et al.*, ASME-MSEC 2018, Texas A&M University, College Station, TX, USA, June 18-22, 2018.

Having implemented the classifier 100 times, an average F-Score of 0.95±0.005 was obtained (α=0.05).

Development of a MISO Classification Model

The performance of the SRC classifier was further contrasted against that of several other classifiers.

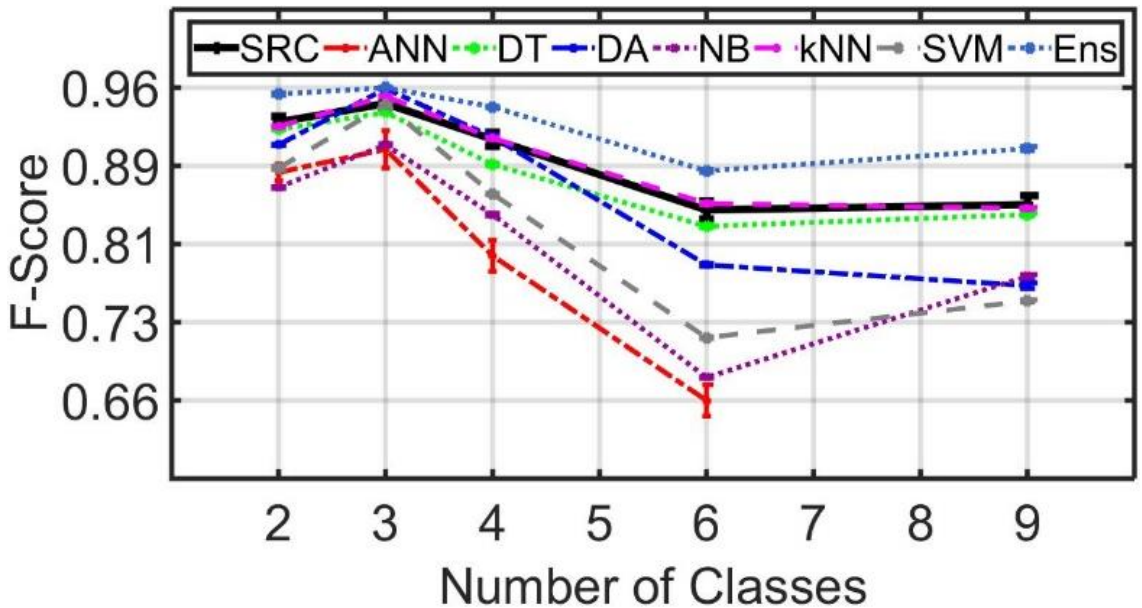

Salary, R., *et al*., ASME-MSEC 2018, Texas A&M University, College Station, TX, USA, June 18-22, 2018.

The SRC classifier appears to be relatively robust and accurate, being among high-performance classifiers.

Summary

AJP is an additive manufacturing (AM) technique, utilized for the fabrication of a broad range of electronic devices.

AJP is intrinsically unstable and prone to gradual drifts in machine behavior and deposited material.

The goal of this work was to realize near real-time functional monitoring of AJ-printed electronic devices.

The Optomec AJP setup was integrated with a high-resolution imaging system, allowing for *in situ* image acquisition.

2D and 3D image-based quantifiers were subsequently introduced to capture various aspects of line morphology.

A CFD model was developed to explain the complex aerodynamics behind aerosol transport and deposition in AJP.

At high ShGFRs, pressure builds up in the head, leading to uneven aerosol deposition and poor line quality.

A novel MIMO classification approach (based on SRC) was forwarded to estimate device functional properties.

It was demonstrated that using the learning model, line resistance could be predicted *in situ* with an accuracy of ≥ 90%.

Acknowledgement

This material is based upon work supported, in part, by Air Force Research Laboratory under agreement number FA8650-15-2-5401. The U.S. Government is authorized to reproduce and distribute reprints for Governmental purposes notwithstanding any copyright notation thereon. The views and conclusions contained herein are those of the authors and should not be interpreted as necessarily representing the official policies or endorsements, either expressed or implied, of Air Force Research Laboratory or the U.S. Government.

The authors would also like to sincerely acknowledge the Small Scale Systems Integration and Packaging (S^3IP) as well as the Center for Advanced Microelectronics Manufacturing (CAMM) at State University of New York (SUNY) at Binghamton.

Contact

Speaker: Roozbeh (Ross) Salary
Ph.D. Candidate and Graduate Research Assistant
Center for Advanced Microelectronics Manufacturing
Department of Systems Science & Industrial Engineering
Thomas J. Watson School of Engineering and Applied Science
State University of New York at Binghamton
Binghamton, NY 13902-6000, USA
Phone: (315)395-4598
E-mail: rsalary1@binghamton.edu

Advisor: Mark D. Poliks, Ph.D.
Empire Innovation Professor of Engineering
Materials Science & Engineering Program
Professor, Systems Science and Industrial Engineering
Director, Undergraduate Studies, ISE Program
Thomas J. Watson School of Engineering & Applied Science
Director, Center for Advanced Microelectronics Manufacturing
Chair, Smart Energy Transdisciplinary Area of Excellence
Phone: 607-727-7104
E-mail: mpoliks@binghamton.edu
Web (CAMM): https://www.binghamton.edu/camm
Web (SSIE): https://www.binghamton.edu/ssie